

Electronic Supplementary Information for
**Redox Chemistry of CeO₂ Nanoparticles in Aquatic Systems
Containing Cr(VI)(aq) and Fe²⁺ Ions**

Jessica R. Ray,[†] Xuanhao Wu, Chelsea Neil,[‡] Haesung Jung,[§] Zhichao Li, and Young-Shin
Jun*

*Department of Energy, Environmental & Chemical Engineering,
Washington University in St. Louis, St. Louis, MO 63130*

E-mail: ysjun@seas.wustl.edu

Phone: (314) 935-4539

Fax: (314) 935-7211

Submitted: April 2019

Environmental Science: Nano

*To Whom Correspondence Should be addressed

[#]Current address: Department of Civil & Environmental Engineering, University of Washington,
Seattle, WA 98195

[‡]Current address: Earth and Environmental Sciences Division, Los Alamos National Laboratory,
Los Alamos, NM 87545, USA

[§] Current address: School of Earth and Atmospheric Sciences, Georgia Institute of Technology,
Atlanta, GA 30332, USA

Summary: Total of fifteen pages with five tables, seven figures and references.

reaction system	CeO ₂ (mg/L)	NaCl (mM)	Fe ²⁺ (mM)	Cr(VI) (mM)
CeO ₂	49	10	0	0
CeO ₂ +Fe ²⁺	48.50	10	0.1	0
CeO ₂ +Fe ²⁺ +Cr	48.00	10	0.1	0.001
CeO ₂ +Fe ²⁺ +5Cr	44.89	10	0.1	0.005
CeO ₂ +5Cr	46.50	10	0	0.005

Table S1. Concentrations of CeO₂, NaCl, Fe²⁺, and Cr(VI) used in each reaction system.

Table S2. XPS reference binding energies and calculated percentages of each corresponding bond at different conditions for O 1s.¹⁻⁷ The area percentages of each peak have a standard deviation of $\pm 2\%$. The “hydroxyl-like groups” in the **CeO₂** system correspond to the presence of –OH groups on CeO₂ NP surfaces.⁷

	Peak area (%)			
	lattice oxygen 529.1 eV	CO ₃ ²⁻ 530.5 eV	hydroxyl-like groups 531.5 eV	adsorbed H ₂ O 532.3 eV
CeO₂ control	74.08	8.78	12.80	4.34
CeO₂+Fe²⁺	66.60	6.48	24.29	2.63
CeO₂ +Fe²⁺+Cr	41.12	5.35	13.80	39.73
CeO₂ +Fe²⁺+5Cr	53.39	5.57	18.59	22.45

Table S3. XPS reference binding energies, area% for each peak, and calculated ratios of Fe²⁺/Fe³⁺ for Fe 2p.⁸⁻¹⁰ The area percentages of each peak have a standard deviation of $\pm 2\%$.

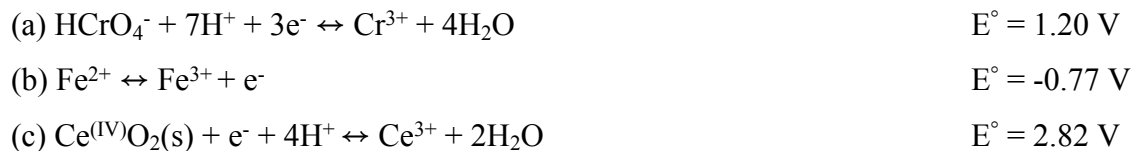
	Peak area (%)							Fe ²⁺ /Fe ³⁺ ratio	Fe/Ce ratio
	Fe 2p _{3/2}		Fe 2P _{3/2} satellites		Fe 2P _{1/2}		Fe 2P _{1/2} satellites		
	Fe ²⁺ 709.9 eV	Fe ³⁺ 711.5 eV	Fe ²⁺ 713.8 eV	Fe ³⁺ 719.3 eV	Fe ²⁺ 723.1 eV	Fe ³⁺ 725.5 eV	Fe ²⁺ 729.0 eV		
CeO₂+Fe²⁺	2.94	1.78	5.90	2.37	1.97	0	5.10	3.88	0.25
CeO₂ +Fe²⁺+Cr	12.05	6.15	7.83	3.36	2.21	0	3.07	2.65	0.53
CeO₂ +Fe²⁺+5Cr	7.15	15.81	4.68	6.23	3.44	0.55	2.15	0.77	0.67

Table S4. XPS reference binding energies, areas% for each peak, and calculated percentages of Ce(III) at different conditions for Ce 3d.^{7, 11, 12} The calculated Ce(III)% has a standard deviation of $\pm 2\%$ based on the variation of area percentages of each peak.

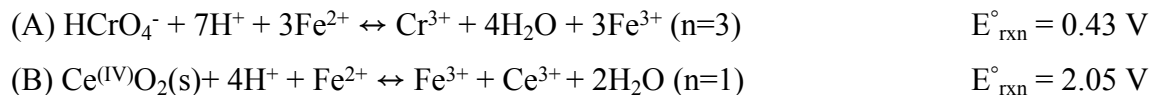
	Peak area (%)							Ce(III) %
	U''	U'	U	V'''	V''	V'	V	
	907.1 eV Ce(IV)	902.9 eV Ce(III)	900.7 eV Ce(IV)	898.1 eV Ce(IV)	888.5 eV Ce(IV)	884.5 eV Ce(III)	882.1 eV Ce(IV)	
CeO₂	9.39	8.02	12.38	22.35	14.27	12.20	21.38	20\pm2
CeO₂+Fe²⁺	9.28	11.82	10.36	21.72	12.59	16.13	18.10	28\pm2
CeO₂ +Fe²⁺+Cr	9.94	9.77	10.76	22.39	14.63	15.68	16.83	25\pm2
CeO₂ +Fe²⁺+5Cr	8.44	7.95	11.69	24.19	14.80	13.63	19.31	22\pm2

S1. Redox Reactions

Half Reactions:



Full Reactions:



Gibbs Free Energy Modeling:

Redox calculations and thermodynamic equilibrium for full reactions (A) and (B) were calculated and modeled using Visual MINTEQ (ver. 3.1).¹³ To calculate the Gibbs free energy, the electrochemical potentials for reactions (A) and (B) were first determined. For reaction (B), we assumed that the $\text{Ce}^{(\text{IV})}\text{O}_2/\text{Ce}^{3+}$ standard reduction potential is the same as the $\text{Ce}^{4+}/\text{Ce}^{3+}$ redox couple to account for the system pH in the thermodynamic calculation to best model our reaction system. For the modeling, the pH was fixed at 5 (the initial pH in the experimental systems) and the ionic strength was fixed at 10 mM for both reactions.

For reaction (A) which models Fe^{2+} oxidation by Cr(VI), the initial concentrations of Fe^{2+} (0.1 mM), Na^+ (10 mM), Cl^- (10 mM), and HCrO_4^- (entered as Cr(VI), 0.001 or 0.005 mM for the $(\text{CeO}_2+)\text{Fe}^{2+}+\text{Cr}$ and $(\text{CeO}_2+)\text{Fe}^{2+}+5\text{Cr}$ system, respectively) were input into the software for the redox reaction calculation. In order to perform the calculations, initial concentrations of Fe^{3+} and Cr^{3+} , the redox reaction products, had to be entered into the software. To include the concentrations, but not heavily influence the calculation, we assumed 1% of the initial Fe^{2+} and Cr(VI) had reacted, which was added as 1 μM Fe^{3+} and 0.01 μM and 0.05 μM Cr^{3+} for the $(\text{CeO}_2+)\text{Fe}^{2+}+\text{Cr}$ and $(\text{CeO}_2+)\text{Fe}^{2+}+5\text{Cr}$ systems, respectively. Note that CeO_2 nanoparticles are not included in the model for these reactions as we are modeling Fe^{3+} formation from the Cr(VI)/ Fe^{2+} redox reaction. In this way, we can better elucidate differences in thermodynamic driving forces for Fe^{2+} oxidation by CeO_2 (examined in reaction (B)) and Cr(VI), separately. The thermodynamic calculations revealed that HCrO_4^- is the dominant Cr(VI) phase in both systems as predicted. The dominant $\text{Cr}^{3+}(\text{aq})$ phase is CrOH^{2+} which could contribute to the $\text{Cr}(\text{OH})_3$ phase formation. While Visual MINTEQ predicts that $\text{Cr}(\text{OH})_3(\text{am})$ phases are undersaturated in both

(CeO₂)+Fe²⁺+Cr and **(CeO₂)+Fe²⁺+5Cr** systems, drying of CeO₂ on silicon wafers and on TEM grids for sample analysis can promote the formation of amorphous Cr(III) hydroxide phases. The Fe(III) phases were all supersaturated with respect to ferrihydrite with the **(CeO₂)+Fe²⁺+5Cr** system exhibiting a larger degree of oversaturation than the **(CeO₂)+Fe²⁺+Cr** system. These results are summarized in Table S3 below.

For the **CeO₂+Fe²⁺** redox calculation, the Ce⁴⁺ (component) and CeO₂ (finite solid phase) had to be added to the Visual MINTEQ database. The solid CeO₂(s) phase solubility product (added as log $K_{sp} = -59.3$)¹⁴ and the Ce⁴⁺ aqueous phase molecular weight (140.116 g/mol) was added as well as the equilibrium constant (i.e., $-\log K = pe^\circ = 47.6$)¹⁵ calculated from the standard half potential for the Ce(IV)/Ce³⁺ half reaction. The initial concentrations of Fe²⁺ (0.1 mM), Na⁺ (10 mM), Cl⁻ (10 mM), and CeO₂ (0.28 mM, calculated from the 48.5 mg/L CeO₂ initial concentration in the **CeO₂+Fe²⁺** system). As before, initial concentrations of Fe³⁺ and Ce³⁺ had to be included to perform the thermodynamic calculation. The product concentrations were added as 1 μ M Fe³⁺ and 28 μ M Ce³⁺ assuming that 1% of the reactants have reacted as with the Fe²⁺/Cr(VI) calculation. The ferrihydrite (Fe(III) phase) was oversaturated in the **CeO₂+Fe²⁺** system as well. The aqueous phase speciation and mineral phase saturation analysis results are summarized in Table S3 below.

Table S5. Summary of the electrochemical potentials (E_h) values, aqueous speciation, and mineral phase identification for reactions (A) and (B) calculated using Visual MINTEQ.

reaction system	E_h (V)	phase	Cr(VI)		Cr(III)		Fe(III)	
			species	% of total ^{*,#}	species	% of total	species	% of total
Fe ²⁺ +Cr	0.443	aqueous	HCrO ₄ ⁻	95.81	CrOH ²⁺	90.58	Fe(OH) ₂ ⁺	93.16
		solid	-	-	Cr(OH) ₃ (am)	undersat.	ferrihydrite	SI = 2.08
Fe ²⁺ +5Cr	0.483	aqueous	HCrO ₄ ⁻	95.73	CrOH ²⁺	90.40	Fe(OH) ₂ ⁺	93.16
		solid	-	-	Cr(OH) ₃ (am)	undersat.	ferrihydrite	SI = 2.68
CeO ₂ +Fe ²⁺	0.407	aqueous					Fe(OH) ₂ ⁺	93.16
		solid					ferrihydrite	SI = 1.47

*aqueous phase calculations are reported as % of the total aqueous species initial concentration.

#solid phase values are reported in terms of saturation. Cr(III) phases were undersaturated (i.e., undersat.), while Fe(III) phases saturation index (SI, log based) are saturated.

Once calculated, the electrochemical potentials for the reactions were used to determine the Gibbs free energy for the formation of Fe^{3+} based on equation (1):

$$\Delta G = -nFEh \quad (1)$$

Our calculations yield the following results:

- A) $\Delta G = -128.48 \text{ kJ}$ (**$\text{Fe}^{2+} + \text{Cr}$** system)
- B) $\Delta G = -139.77 \text{ kJ}$ (**$\text{Fe}^{2+} + 5\text{Cr}$** system)
- C) $\Delta G = -39.31 \text{ kJ}$ (**$\text{CeO}_2 + \text{Fe}^{2+}$** system)

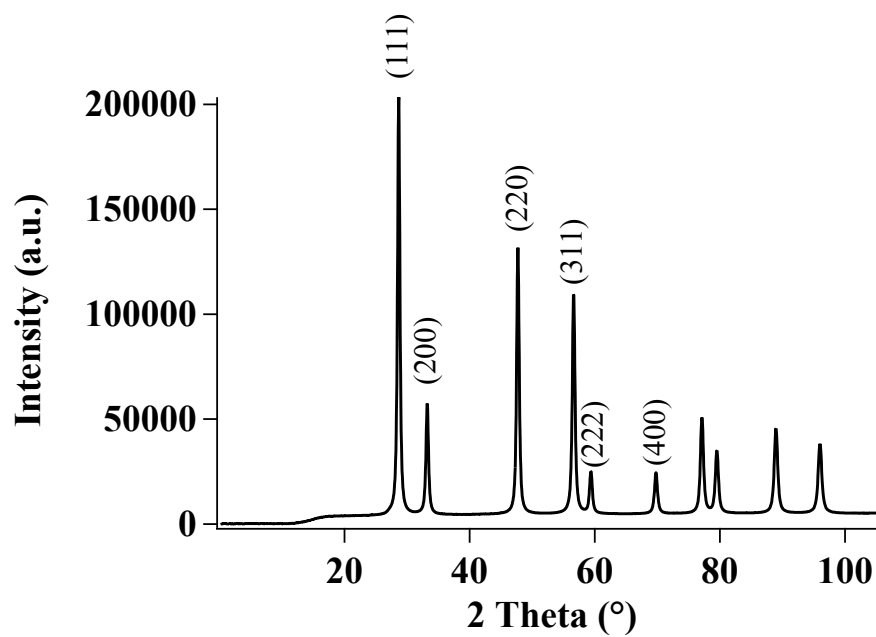


Figure S1. WAXRD spectrum of CeO₂ NPs used in this study. The spectrum recorded matches well with reference CeO₂ diffraction peaks.¹⁶

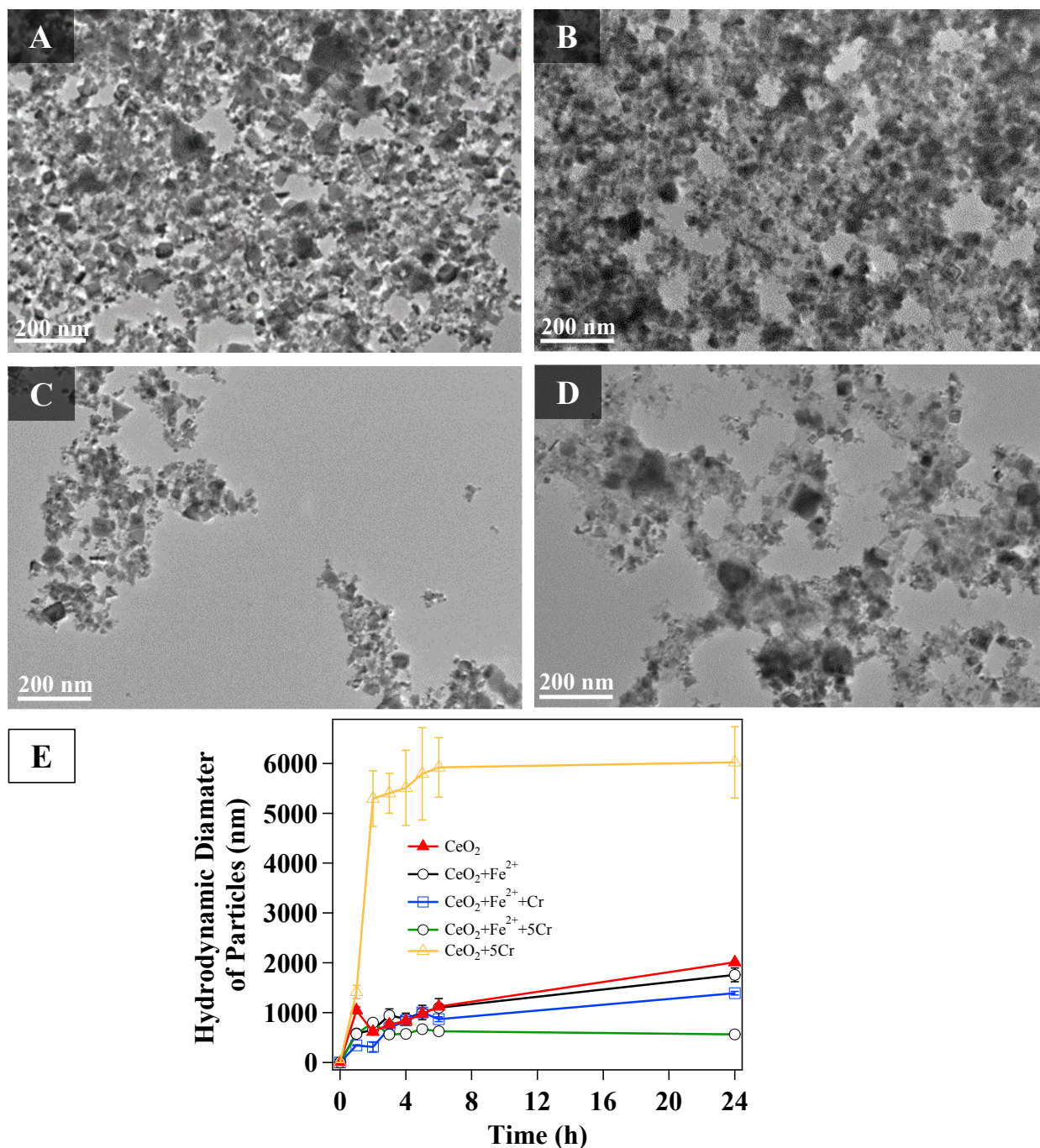


Figure S2. HR-TEM micrographs of (A) CeO_2 , (B) $\text{CeO}_2 + \text{Fe}^{2+}$, (C) $\text{CeO}_2 + \text{Fe}^{2+} + \text{Cr}$, and (D) $\text{CeO}_2 + \text{Fe}^{2+} + 5\text{Cr}$ reaction systems, showing the varying aggregation states in each system. (E) The *in situ* dynamic light scattering (DLS) aggregate hydrodynamic diameter agrees with the *ex situ* HR-TEM micrograph observations.

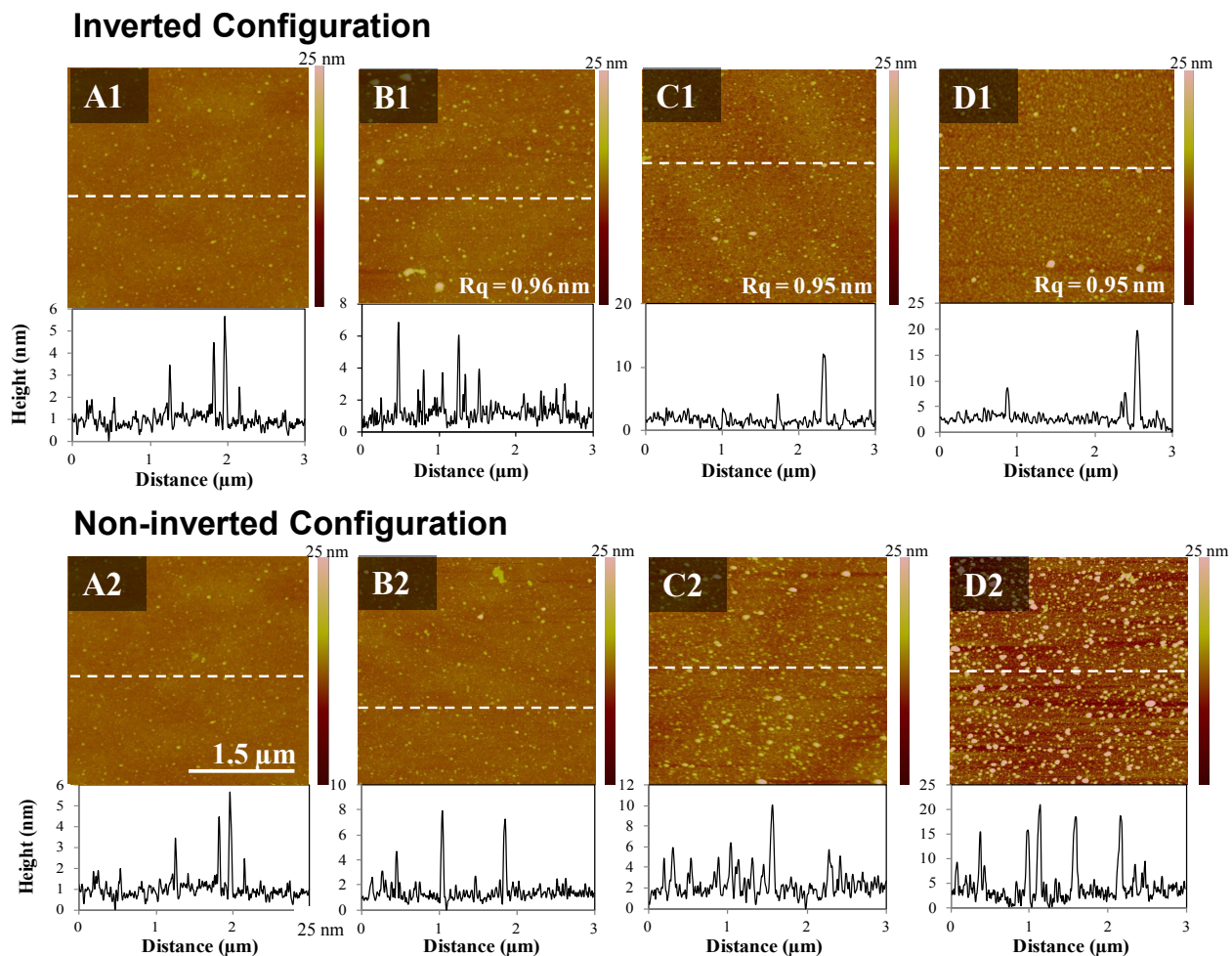
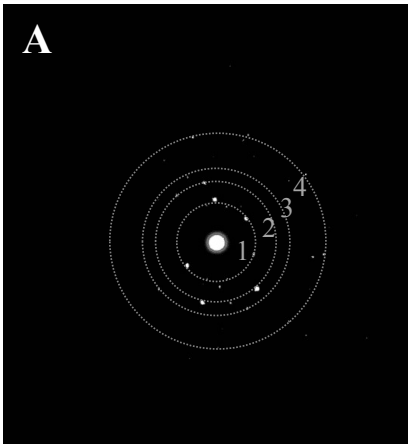


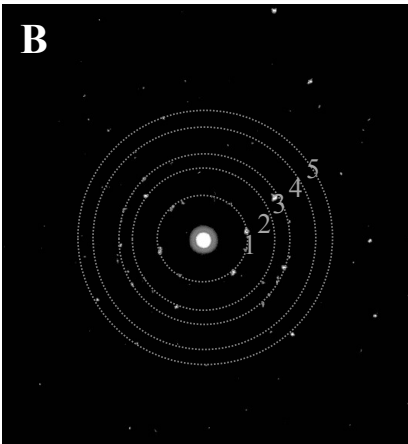
Figure S3. AFM images showing the morphologies of CeO_2 -sputtered wafers after reaction in (A) CeO_2 (i.e., unreacted), (B) $\text{CeO}_2+\text{Fe}^{2+}$, (C) $\text{CeO}_2+\text{Fe}^{2+}+\text{Cr}$, and (D) $\text{CeO}_2+\text{Fe}^{2+}+5\text{Cr}$. The top row (row 1) shows the degree of precipitation in the inverted system configuration, highlighting heterogeneous nucleation, while the bottom row (row 2) shows both hetero- and homogeneous nucleation from the non-inverted system configuration described in the main text. Height cross sections taken across the white dotted line in each figure are given below its corresponding image.

	Measured d-spacing (Å)	Possible match (Å)
(A) CeO₂+Fe²⁺	1.3201 ¹	CeO ₂ (1.3528)
	1.6181 ²	CeO ₂ (1.6315), 6LF (1.6)
	1.7915 ³	CeO ₂ (1.6315), 6LF (1.6)
	2.0901 ⁴	6LF (2.0)
(B) CeO₂+Fe²⁺+Cr	1.3201 ¹	CeO ₂ (1.3528)
	1.6721 ²	CeO ₂ (1.6315), 6LF (1.7)
	2.0901 ³	6LF (2.0)
	2.1810	6LF (2.2)
	2.2801 ⁴	6LF (2.3)
	2.3887 ⁵	6LF (2.3)
(C) CeO₂+Fe²⁺+5Cr	1.5676 ¹	CeO ₂ (1.5620), 6LF (1.6)
	1.6721 ²	CeO ₂ (1.6315), 6LF (1.7), Cr ₂ O ₃ (1.6732)
	1.9293 ³	CeO ₂ (1.9131)
	2.1810	6LF (2.2)
	2.6401 ⁴	Cr ₂ O ₃ (2.6660)

A



B



C

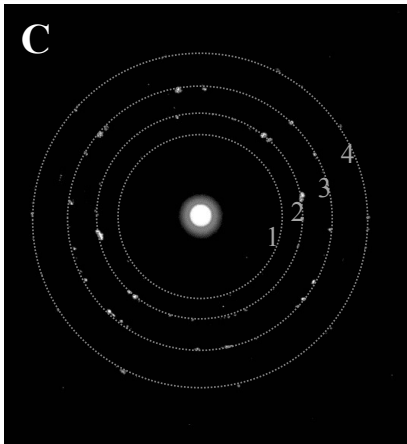


Figure S4. Electron diffraction for the (A) **CeO₂+Fe²⁺**, (B) **CeO₂+Fe²⁺+Cr**, and (C) **CeO₂+Fe²⁺+5Cr** reaction systems and their d-spacing matches with CeO₂, 6-line ferrihydrite

(6LF), and the Cr(III) phase eskolaite (Cr_2O_3). The superscript numbers after the measured d-spacing values for each system correspond to the indexed d-spacing and crystallinity in the appropriate reaction system electron diffraction. Other d-spacings listed in the table were measured, but not clearly visible in the scanned diffraction patterns. The measured d-spacings have a standard deviation of $\pm 7\%$, determined from instrument precision. One caveat of HR-TEM electron diffraction analysis is that it is an *ex situ* characterization technique, and drying during sample preparation could induce precipitation and promote crystallization of amorphous phases. However, the HR-TEM samples were prepared in the same way at the same time, and therefore, the drying effects will be the same for each sample.

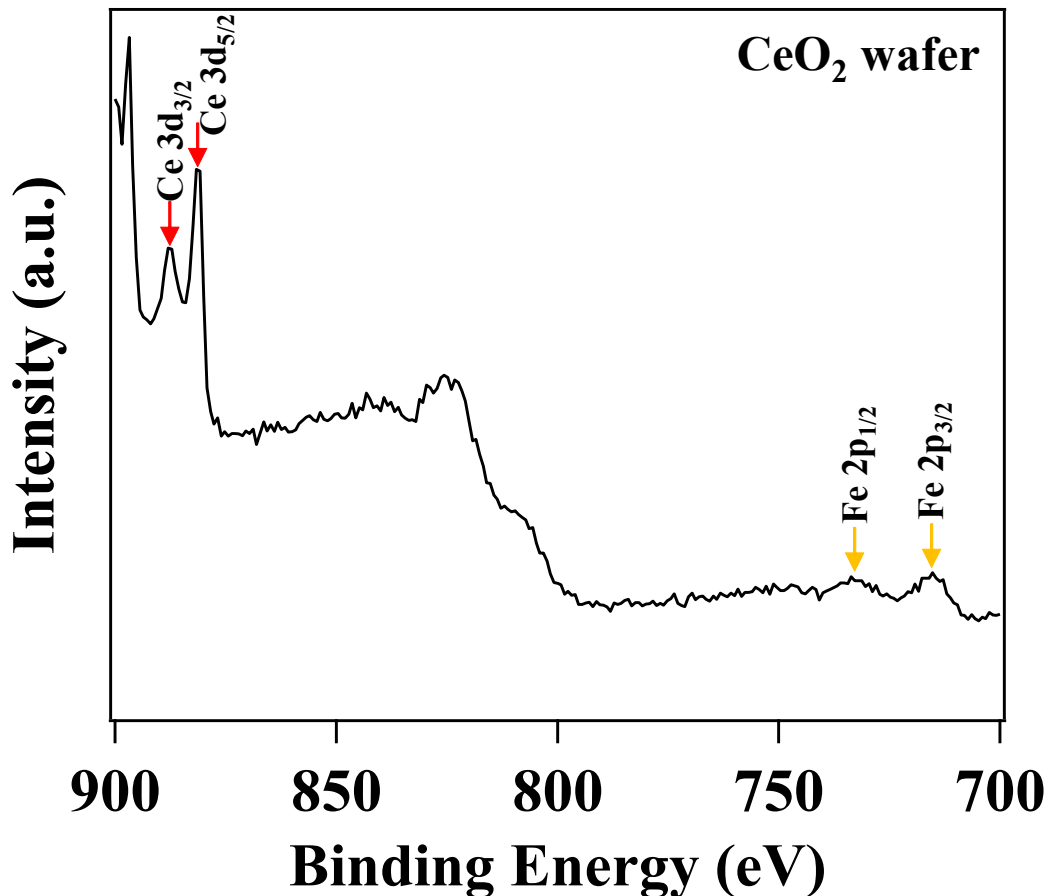


Figure S5. XPS full survey scan for a clean CeO_2 -sputtered Si wafer. While the Ce 3d XPS signal lies within the 875–900 eV range (as seen in Figure S6A), we can also observe peaks in the Fe 2p

spectral range of 700–740 eV. This phenomenon explains the occurrence of apparent Fe 2p peaks for the **CeO₂** system, where no Fe peaks should exist.

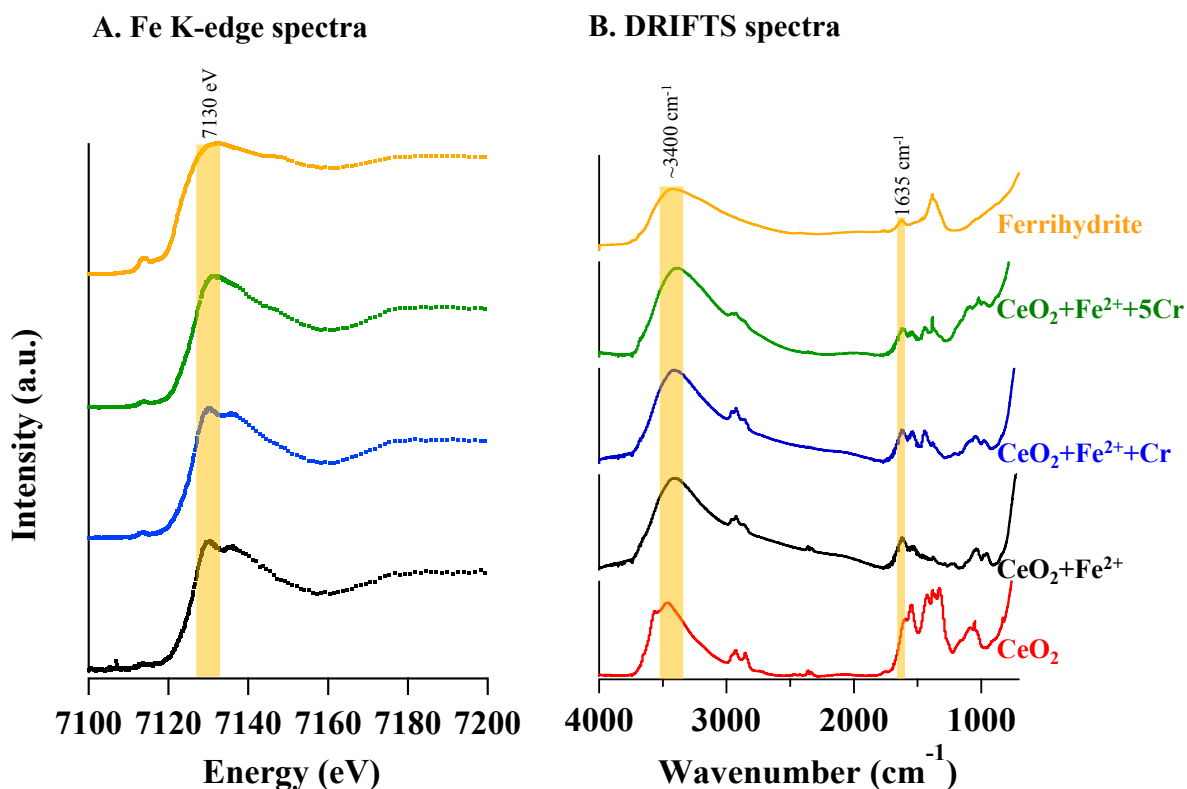


Figure S6. (A) Fe K-edge spectra for the three iron-containing systems ($\text{CeO}_2 + \text{Fe}^{2+}$, $\text{CeO}_2 + \text{Fe}^{2+} + \text{Cr}$, and $\text{CeO}_2 + \text{Fe}^{2+} + 5\text{Cr}$) and a 6LF reference. As the Cr(VI) concentration increases, the ferrihydrite peak at 7130 eV becomes sharper, suggesting greater ferrihydrite content. This observation is consistent with our other experimental findings. (B) Diffuse reflectance infrared Fourier transform spectroscopy (DRIFTS, Praying Mantis accessory, Harric Scientific, NY) IR analyses were conducted for the CeO_2 , $\text{CeO}_2 + \text{Fe}^{2+}$, $\text{CeO}_2 + \text{Fe}^{2+} + \text{Cr}$, and $\text{CeO}_2 + \text{Fe}^{2+} + 5\text{Cr}$ systems and for the ferrihydrite standard. The peak at 1635 cm^{-1} and the broad peak near 3400 cm^{-1} correspond to adsorbed water and to $-\text{OH}$ group stretching in the 6-line ferrihydrite structure, respectively.¹⁷ These peaks in the Fe^{2+} -containing systems suggest the presence of 6LF. Peaks indicating the presence of amorphous $\text{Cr}^{\text{III}}(\text{OH})_3$ phases are in the 400–600 cm^{-1} region¹⁸ which was difficult to resolve in our data due to a noisy signal.

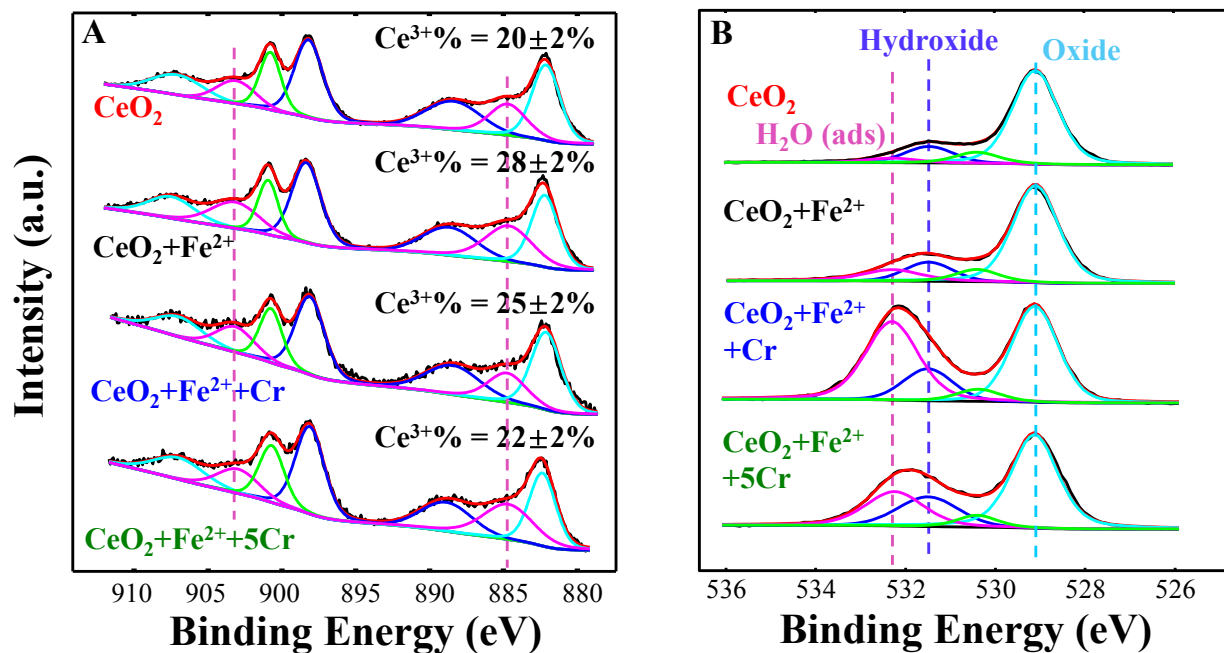


Figure S7. The (A) Ce 3d, and (B) O 1s XPS spectra for the CeO_2 , $\text{CeO}_2 + \text{Fe}^{2+}$, $\text{CeO}_2 + \text{Fe}^{2+} + \text{Cr}$, and $\text{CeO}_2 + \text{Fe}^{2+} + 5\text{Cr}$ systems.

REFERENCES

1. H. Chen, A. Sayari, A. Adnot and F. ç. Larachi, Composition–activity effects of Mn–Ce–O composites on phenol catalytic wet oxidation, *Appl. Catal. B-Environ.*, 2001, **32**, 195-204.
2. S. Hamoudi, F. ç. Larachi, A. Adnot and A. Sayari, Characterization of spent MnO₂/CeO₂ wet oxidation catalyst by TPO–MS, XPS, and S-SIMS, *J. Catal.*, 1999, **185**, 333-344.
3. A. Hughes, R. Taylor, B. Hinton and L. Wilson, XPS and SEM characterization of hydrated cerium oxide conversion coatings, *Surf. Interface Anal.*, 1995, **23**, 540-550.
4. A. Laachir, V. Perrichon, A. Badri, J. Lamotte, E. Catherine, J. C. Lavalley, J. El Fallah, L. Hilaire, F. Le Normand and E. Quéméré, Reduction of CeO₂ by hydrogen. Magnetic susceptibility and Fourier-transform infrared, ultraviolet and X-ray photoelectron spectroscopy measurements, *J. Chem. Soc. Faraday T.*, 1991, **87**, 1601-1609.
5. G. Pirug, C. Ritke and H. Bonzel, Adsorption of H₂O on Ru (001): I. Bilayer and clusters, *Surf. Sci.*, 1991, **241**, 289-301.
6. F. Scholes, A. Hughes, S. Hardin, P. Lynch and P. Miller, Influence of hydrogen peroxide in the preparation of nanocrystalline ceria, *Chem. Mat.*, 2007, **19**, 2321-2328.
7. X. Wu, C. W. Neil, D. Kim, H. Jung and Y.-S. Jun, Co-effects of UV/H₂O₂ and natural organic matter on the surface chemistry of cerium oxide nanoparticles, *Environ. Sci.-Nano*, 2018, **5**, 2382-2393.
8. M. Aronniemi, J. Sainio and J. Lahtinen, Chemical state quantification of iron and chromium oxides using XPS: the effect of the background subtraction method, *Surf. Sci.*, 2005, **578**, 108-123.
9. M. Descostes, F. Mercier, N. Thromat, C. Beaucaire and M. Gautier-Soyer, Use of XPS in the determination of chemical environment and oxidation state of iron and sulfur samples: constitution of a data basis in binding energies for Fe and S reference compounds and applications to the evidence of surface species of an oxidized pyrite in a carbonate medium, *Appl. Surf. Sci.*, 2000, **165**, 288-302.
10. T.-C. Lin, G. Seshadri and J. A. Kelber, A consistent method for quantitative XPS peak analysis of thin oxide films on clean polycrystalline iron surfaces, *Appl. Surf. Sci.*, 1997, **119**, 83-92.
11. S. Deshpande, S. Patil, S. V. Kuchibhatla and S. Seal, Size dependency variation in lattice parameter and valency states in nanocrystalline cerium oxide, *Appl. Phys. Lett.*, 2005, **87**, 133113.
12. F. Zhang, P. Wang, J. Koberstein, S. Khalid and S.-W. Chan, Cerium oxidation state in ceria nanoparticles studied with X-ray photoelectron spectroscopy and absorption near edge spectroscopy, *Surf. Sci.*, 2004, **563**, 74-82.

13. KTH, Visual MINTEQ, 2013. Free Version, Department of Land and Water Resources Engineering, <https://vminteq.lwr.kth.se/>, 2016).
14. R. Li, Z. Ji, C. H. Chang, D. R. Dunphy, X. Cai, H. Meng, H. Zhang, B. Sun, X. Wang, J. Dong, S. Lin, M. Wang, Y.-P. Liao, C. J. Brinker, A. Nel and T. Xia, Surface Interactions with Compartmentalized Cellular Phosphates Explain Rare Earth Oxide Nanoparticle Hazard and Provide Opportunities for Safer Design, *ACS Nano*, 2014, **8**, 1771-1783.
15. D. L. Sparks, *Environmental Soil Chemistry*, Elsevier Science, 2013.
16. C. Sun, H. Li, H. Zhang, Z. Wang and L. Chen, Controlled synthesis of CeO₂nanorods by a solvothermal method, *Nanotechnol.*, 2005, **16**, 1454-1463.
17. L. Mazzetti and P. J. Thistlethwaite, Raman spectra and thermal transformations of ferrihydrite and schwertmannite, *J. Raman Spectrosc.*, 2002, **33**, 104-111.
18. S. Music, M. Maljkovic, S. Popovic and R. Trojko, Formation of chromia from amorphous chromium hydroxide, *Croat. Chem. Acta*, 1999, **72**, 789-802.